

# Droplet mobility manipulation on porous media using backpressure

*N. Vourdas<sup>1</sup>, G. Pashos<sup>2</sup>, G. Kokkoris<sup>2,3</sup>, A.G. Boudouvis<sup>2</sup> and V.N. Stathopoulos<sup>1</sup>*

<sup>1</sup>School of Technological Applications, Technological Educational Institute of Sterea Ellada, Psahna 34400, Evia, Greece

<sup>2</sup>School of Chemical Engineering, National Technical University of Athens, Zografou Campus, Athens 15780, Greece

<sup>3</sup>Institute of Nanoscience & Nanotechnology, NCSR Demokritos, Athens 15310, Greece

## ABSTRACT

Wetting phenomena on hydrophobic surfaces are strongly related to the volume and the pressure of gas pockets, resided at the solid-liquid interface. In this study we explore the underlying mechanisms of droplet actuation and mobility manipulation, when backpressure is applied through a porous medium under a sessile pinned droplet. Reversible transitions between the initially sticky state and the slippery states are thus incited, by modulating the backpressure. Sliding angle of deionized (DI) water as well as ethanol in DI water droplets of various volumes are presented to quantify the effect of the backpressure on the droplet mobility. For a 50  $\mu$ l water droplet the sliding angle decreases from 45° to 0° when the backpressure increases to ca. 0.60 bar. Significantly smaller backpressure levels are required for lower surface energy liquids. We shed light on the

droplet actuation and movement mechanisms by means of simulations encompassing the momentum conservation and the continuity equations along with the Cahn-Hilliard phase-field equations in a 2D computational domain. The droplet actuation mechanism entails depinning of the receding contact line and movement, by means of a forward wave propagation reaching on the front of the droplet. Eventually, the droplet is skipping forward. The contact line depinning is also corroborated by analytical calculations based on the governing vertical force balance, properly modified to incorporate the effect of the backpressure.

**Keywords:** droplet actuation, droplet mobility, porous surfaces, slippery surfaces

## INTRODUCTION

Control over the mobility of droplets on surfaces remains an important part of recent research activity, both for understanding the pertaining wetting principles<sup>1</sup> as well as for practical applications including open, closed and digital microfluidics and related technologies<sup>2, 3, 4, 5, 6, 7, 8</sup>, chemical processes in droplets<sup>9, 10</sup>, engineered self-cleaning surfaces<sup>11, 12, 13, 14</sup>, antiicing coatings<sup>15</sup>,<sup>16</sup>, membrane contactors<sup>17</sup>, polymer electrolyte fuel cells<sup>18, 19</sup>, heat exchangers<sup>20, 21</sup> etc.

In this direction a variety of approaches have been proposed towards preparing “active”<sup>22</sup>, or “tunable”<sup>23</sup>, or “adaptive”<sup>24</sup>, or “skating-like”<sup>25</sup> surfaces, namely manipulating the mobility of a droplet or a liquid film, mainly based on the respective wetting transitions. Pertinent methodologies have been reviewed recently<sup>26, 27, 28, 29, 30</sup>.

The vast majority of the methods for active droplet mobility manipulation entails the use of electrical<sup>31</sup>, magnetic<sup>32</sup>, thermal<sup>33</sup>, vibrational<sup>34, 35, 36</sup>, mechanical<sup>37</sup>, or optical stimuli<sup>38</sup> and necessitates fabrication of microelectrodes, or specific stacking layer sequences or surface

texturing, requires structures with flexural elasticity, induce heat dissipation, or introduce foreign particles in the liquid phase which may provide drawbacks for specific applications.

Particular interest has been attracted by some active methods interfering directly with the volume and the pressure of the gas pockets resided in the textured solid-liquid interface; such characteristics are crucial in such phenomena<sup>39</sup>. The presence of a thin “lubricating air film” under the liquid has proven to play a major role in the mobility of droplets e.g. after impingement on rough<sup>40</sup> or porous<sup>41</sup> surfaces, as well as on liquids<sup>42</sup>. Moreover the pressure difference below and over the droplet has been identified as critical in spontaneous droplet depinning<sup>43</sup>. Pertinent direct approaches for tuning the gas pockets have found various applications such as in underwater restoration of superhydrophobicity<sup>44</sup> through electrochemical gas production or in writing/erasing procedures<sup>45</sup>, enabling storage of binary data, by producing an over- or under-pressure through an orifice.

Alternatively, the gas pockets may also be produced and tuned through direct pressure application from the rear side (backpressure), by ejecting gas through one hole<sup>41, 46, 47</sup>, or by introducing gas bubbles by means of a pipette<sup>48, 49, 50, 51</sup>. The limit of this process is the case of drops levitated by an air cushion by an air stream flowing under a droplet<sup>27, 52, 53, 54, 55</sup>.

In this direction we have recently developed a method for droplet actuation and mobility manipulation on porous media<sup>56, 57, 58</sup>, which has found application in open-channel fluidic valving<sup>59, 60</sup>, and in mobility control after impingement<sup>41</sup>. Contrary to the droplets levitated by an air cushion exhibiting a frictionless mobility, our method provokes only partial depinning of the solid-liquid interface, which is enough to render the droplet mobile and to incite a downward movement. The main advantages of this include the absence of moving parts and the circumvent of electrical, magnetic, optical, vibrational, and acoustical stimuli on the surface. The heat dissipation may be not only minimized but also finely controlled, e.g. by controlling the

temperature of the gas feed. Introduction of foreign particles/molecules in the working liquid/droplet is completely avoided. It may accommodate various liquids, i.e. may work on deionized (DI) water to aqueous solutions, as will be evidenced hereafter, and is amenable for integration on devices for active control. Finally the response time is ultra-low, in the order of some ms, and if appropriate microporous structure is selected, its energy demands are significantly lower compared to the other methods.

Even though this method has been proven rather versatile in delivering mobility manipulation, as described above, we have not yet provided the underlying working mechanism. The application of the backpressure introduces a variety of changes<sup>51</sup> in wetting-related parameters, such as in the advancing and mainly in the receding contact angle and in the liquid-solid contact area. Additional Laplace forces appear, which are asymmetric due to the inclination, and deform the droplet shape. The air cushion under the droplet is not fully developed, and therefore Leidenfrost dynamics<sup>61, 62</sup> are not suitable to apply. For this reason we may not assume that the droplet is supported on air-like lubricating film<sup>63</sup>, i.e. the air pockets do not fully bear the gravitational force exerted by the droplet. On the other hand, the droplet does not attain a Wenzel, i.e. fully wetted, state and therefore well-established Wenzel to Cassie-Baxter, i.e. partially wetted, transition dynamics are not pertinent. The droplet moves along various Cassie-Baxter states enabled by the application of backpressure; some of which correspond to a sticky behavior and some to slippery behavior. Moreover a model accounting the downward force exerted by each bubble, alone, has been proven to be inadequate<sup>51</sup>.

In this work we shed light on the underlying working mechanisms of droplet actuation and movement induced by backpressure application through a porous medium. The problem is followed by means of simulations encompassing the momentum conservation and the continuity equations along with the Cahn-Hilliard phase-field equations in a 2D domain and by employing

the governing vertical force balance accounting for the partial depinning of the receding contact line. This depinning is also corroborated by analytical calculations. The pertaining vertical force balance has been modified to incorporate the effect of the backpressure and to yield the pinned fraction of the contact line. The results from the theoretical approach are compared to the experimental observations, thus providing a reasonable understanding of the respective droplet actuation and movement mechanisms.

## **EXPERIMENTAL**

Porous media (membranes) were fabricated from  $\alpha$ -Al<sub>2</sub>O<sub>3</sub> powder, with a particle size distribution, in which the 90% of the particles had diameter less than 7.0  $\mu\text{m}$ , i.e.  $D_{0.9}=7.1 \mu\text{m}$ . (NH<sub>4</sub>)<sub>2</sub>HPO<sub>4</sub> was added to Al<sub>2</sub>O<sub>3</sub> powder as much as 5%wt and the mixture was uniaxially pressed under 110 MPa to form green disk-shaped membranes with diameter of 13 mm. A similar procedure was followed to form membranes with diameter of 32 mm. The final membranes were prepared after sintering the green samples for 3 h at 1000 °C. At this stage, the membranes are superhydrophilic and water absorbing. The applicability of this method is not limited to this porous structure. Other porous materials may be used with various optical, structural, and electrical characteristics as well<sup>64, 65</sup>.

To render the initially superhydrophilic and water absorbing surface into a hydrophobic one, all the membranes were infiltrated with 0.5%wt Teflon solution (poly(4,5-difluoro-2,2-bis(trifluoromethyl)-1,3-dioxole-co-tetrafluoroethylene in Fluorinert FC-770) and then heated up to 110 °C for 20 min. SL200KS from Kino was used to measure the contact angle after this treatment. The apparent contact angle was ca. 122° and ca. 45° for the water and the 7.5% ethanol (mole fraction) in water, respectively, measured with 5  $\mu\text{l}$  droplets. Experiments have been also performed on membranes deposited via vapor deposition with appropriate precursor to deliver grafting of self-assembled perfluorododecyltrichlorosilane monolayers (SAMs).

Scanning Electron Microscopy (SEM) image of the  $D_{0.9}=7.1 \mu\text{m}$  hydrophobic membrane, i.e. after Teflon coating, is presented in Figure 1.

Measurement of the average pore size and spacing may not be straightforward in such surfaces. Pores cannot be explicitly defined, and their size depends on the actual wetted fraction area, information which cannot be predicted in advance, as e.g. in the case of lithographically fabricated structures. A detailed discussion on this may be found in a previously published study<sup>41</sup>. In any case, the scale of geometrical characteristics of the surface is well lower compared to the nominal wetted area. For the analytical approach, presented below, pore radius values varied from ca.  $0.5 \mu\text{m}$  to ca.  $1.6 \mu\text{m}$ , and contact patch radius from ca.  $0.50 \mu\text{m}$  to  $1.65 \mu\text{m}$ .

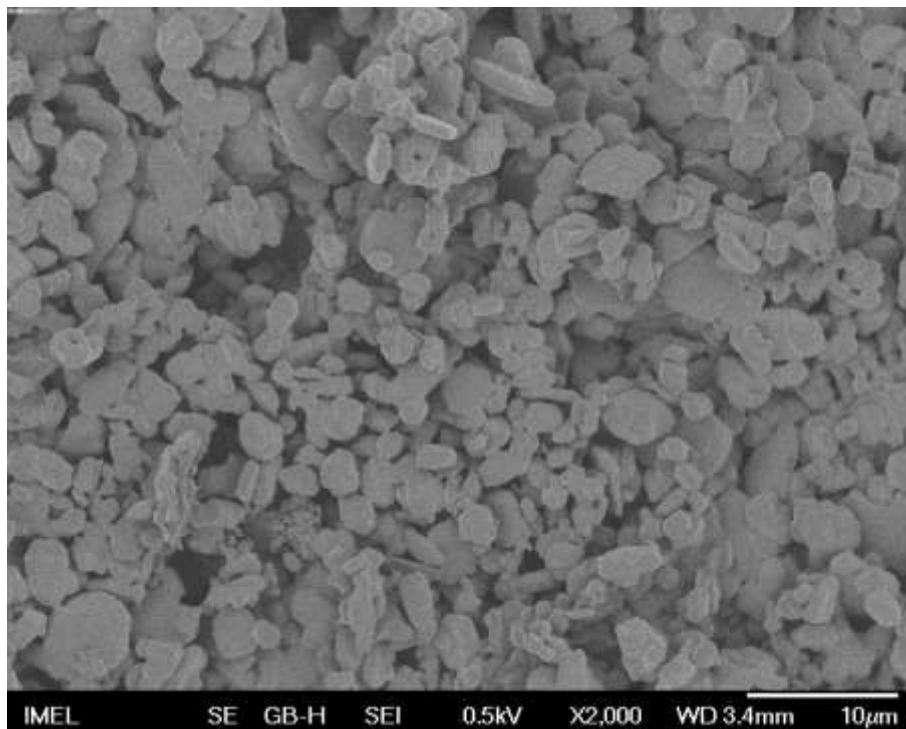


**Figure 1.** SEM image of the hydrophobic porous medium surface ( $\alpha\text{-Al}_2\text{O}_3$ ,  $D_{0.9}=7.1 \mu\text{m}$ ).

The hydrophobic porous medium was positioned on a perforated plexiglas sheet under which the gas pressure is controlled using needle valve and a manometer with accuracy of  $\pm 2$  mbar, from KIMO (Model MP 200HP). A schematic representation of the experimental setup is given in Figure 2. In all cases presented herein compressed air was used as the pneumatic means for actuation and mobility manipulation.

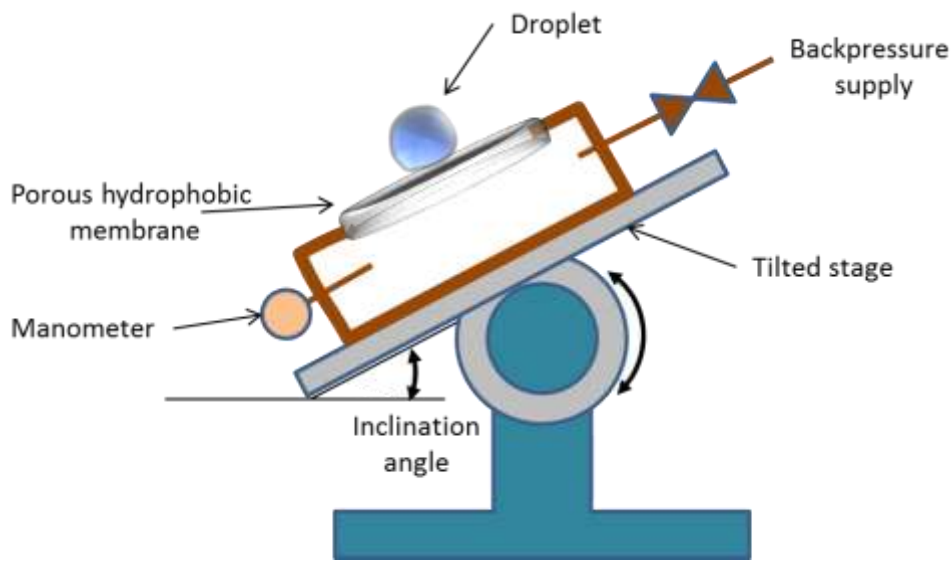


**Figure 2.** Schematic representation of the experimental setup used for the measurement of the sliding angle ( $\alpha$ ) variation with backpressure. The sliding angle is the minimum inclination angle at which the droplet moves systematically downwards.

## EXPERIMENTAL RESULTS AND DISCUSSION

In Figure 3 the sliding angle of water droplets of various volumes are presented vs. the applied backpressure on the porous surface. The sliding angle ( $\alpha$ ) is defined as the minimum tilt angle at which the droplet moves systematically downwards, at a particular backpressure for each droplet volume. The droplet was first positioned on the porous surface and then the backpressure was

gradually increased up to the point where sliding took place. Increase of the backpressure incites partial droplet depinning, as will be discussed later thus decreasing the sliding angle. After this step the gravitational force,  $F_G$ , induces a downward movement of the droplet. It is expected that as  $F_G$  increases, less pronounced depinning is needed to induce movement, i.e. the depinning fraction may be lower. We note here, and will discuss later, that at this limit backpressure the sliding takes place in a stick-slip kind of movement, i.e. the droplet does not move downwards continuously.

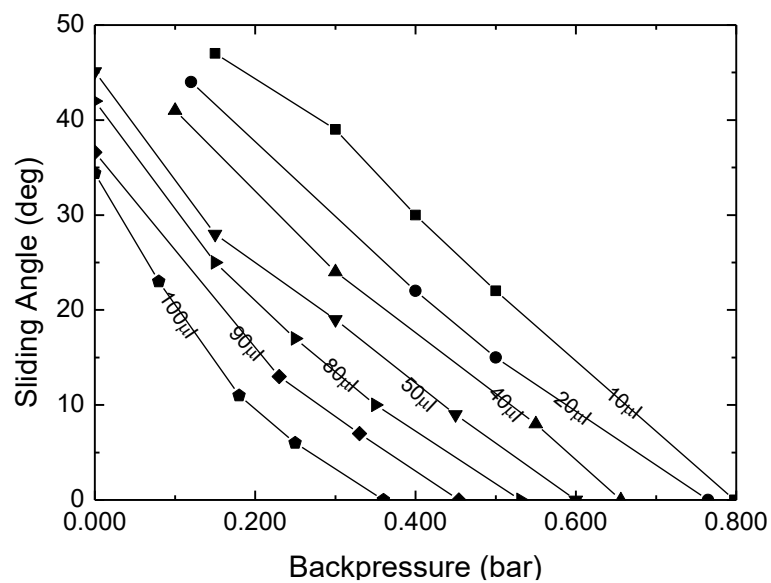


**Figure 3.** Variation of sliding angle ( $\alpha$ ) with backpressure. Lines of different DI water droplets volumes are depicted.

The sliding angle of a 50  $\mu\text{l}$  water droplet is  $45^\circ$ , when no backpressure is applied and gradually drops to  $28^\circ$  and  $10^\circ$  when the backpressure increases to 0.17 and 0.43 bar, respectively. When the backpressure increases to 0.60 bar the 50  $\mu\text{l}$  water droplet exhibits high mobility and eventually slides outside the membrane.

This case has been photo captured and presented as a sequence of snapshots in Figure 4a. Initially the droplet is impaled on the surface. Upon the backpressure application multiple gas pockets appear on the liquid-solid interface, deforming the droplet and gradually inciting downward movement. Not all of the gas pockets are of the same volume; some evolve faster than other, some coalesce with each other etc. As seen in Figure 4a, the droplet is not completely levitated throughout the process. Of particular interest are the small openings at the contact line, as seen e.g. in Figure 4a (III)-(IV). These are gas pockets resided near the contact line and break the contact line; with the gas flow these openings are sustained or evolving up until the droplet moves. In some cases, mostly for large droplets and high backpressure values small ejected droplets may appear, as in Ref.<sup>66</sup>

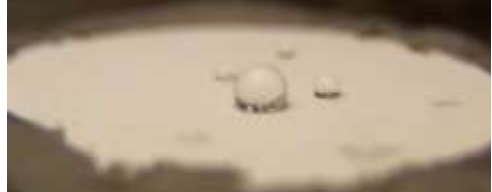
(I)



(II)



(III)



(IV)



(V)



(VI)



(VII)



(VIII)



(a)

(b)

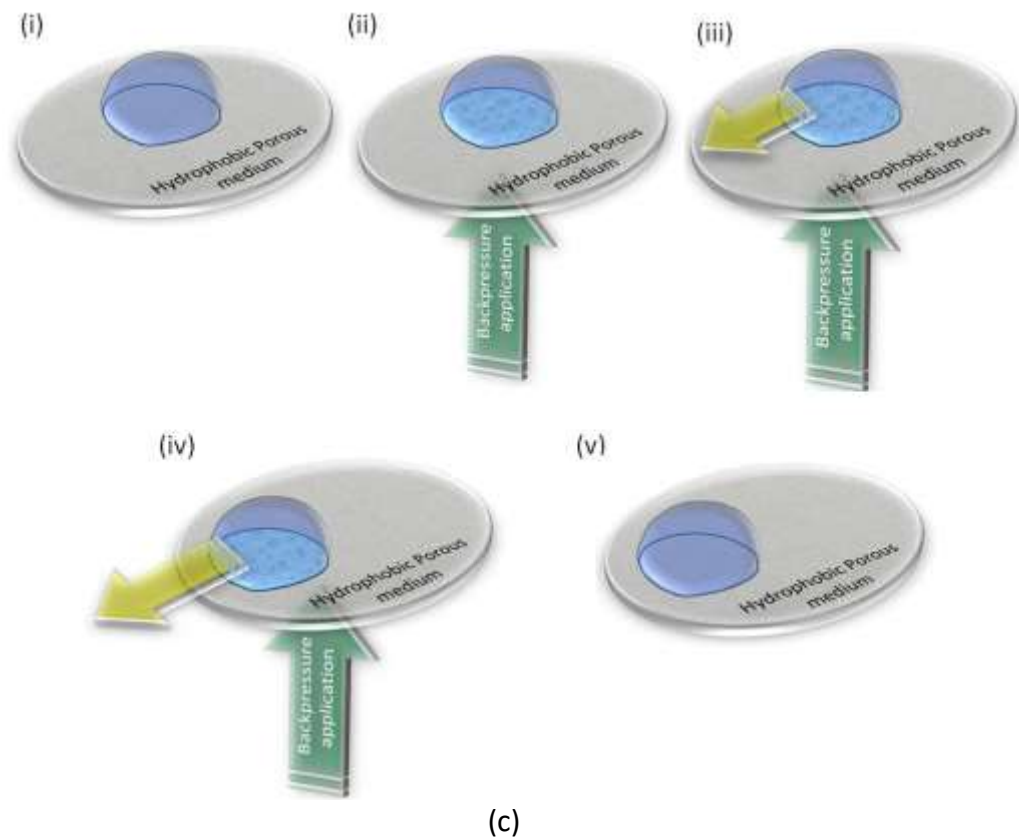


**Figure 4.** Water droplets upon backpressure application on a porous medium (a)  $V=60\ \mu\text{l}$  and (b)  $V=20\ \mu\text{l}$ . For large droplets multiple air pockets appear at the liquid-solid interface, whereas for the smaller droplets one pocket finally evolves leveraging the droplet sliding. In (b) smaller droplets are not moving, indicating that the actuation is volume-sensitive. (c) Schematic representation of the droplet actuation and mobility manipulation. (i) A quiescent droplet on an inclined surface, (ii) backpressure application and gas pocket appearance, resulting instantly in (iii) droplet actuation, (iv) droplet movement, and (v) the surface becomes sticky again when no backpressure is applied.

Droplets with volume lower than  $40\ \mu\text{l}$  do not slide even at  $90^\circ$  angle, when no backpressure is applied. The inherently sticky surface gradually becomes slippery for a  $40\ \mu\text{l}$  droplet upon  $0.11$  bar backpressure application, exhibiting a sliding angle of  $42^\circ$ . At backpressure equal to  $0.65$  bar the droplet exhibits high mobility, even at a horizontal porous surface. Similar behavior is recorded

for the 20 and 10  $\mu\text{l}$  droplet. For small droplets ( $V < 40 \mu\text{l}$ ) one gas pocket is evolved under the liquid phase, thus providing the adequate lubrication for the droplet to slide. However this air cushion is not fully developed as the one observed in Leidenfrost phenomena<sup>61</sup>.

This method for actuation and mobility manipulation may also be used for droplets of lower surface energy. In Figure 5 we present the sliding angle variation of a 7.5% ethanol (mole fraction) in water droplets vs. the applied backpressure. This solution exhibits surface tension of ca. 0.045 N/m, i.e. lower than water exhibiting 0.073 N/m.

Again the sliding angle decreases with the backpressure and with the droplet volume. However, in this case, the backpressure levels to render the surface slippery are lower compared to DI water. A 40  $\mu\text{l}$  ethanol in water droplet becomes slippery in ca. 0.14 bar in a horizontal surface, whereas for a DI water droplet a backpressure of 0.65 bar was needed. Again we did not observe a fully developed air cushion under the liquid.

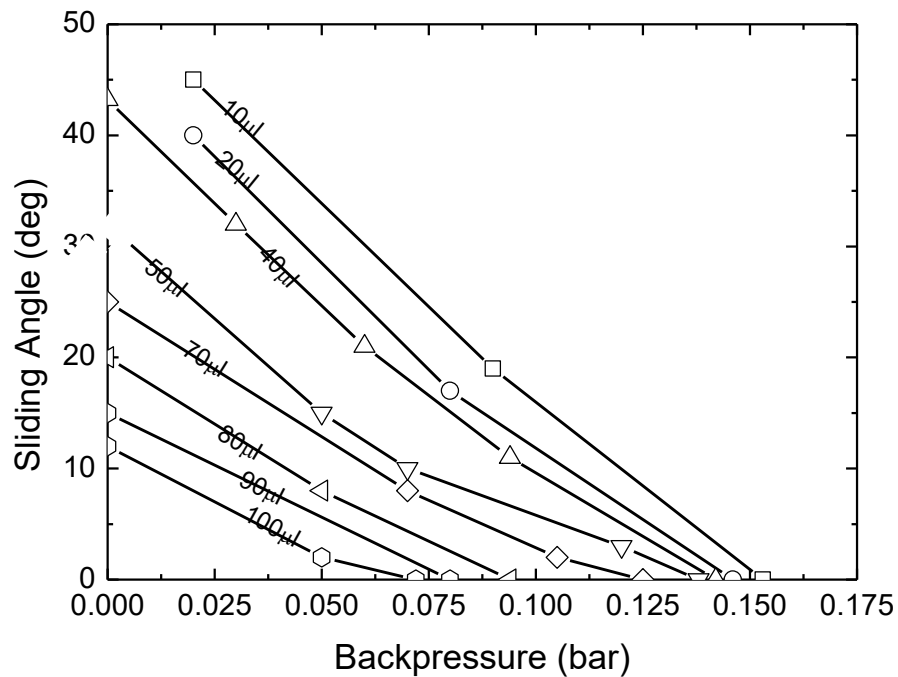


**Figure 5.** Sliding angle variation of 7.5% (mole fraction) ethanol in water droplets vs. backpressure

In all cases, both for large and small water droplets, as well as for lower surface energy droplets the mobility switching is reversible, i.e. upon backpressure relief, the surface returns to a sticky state and the droplet pins to it. Again after backpressure application the droplet is again actuated as described before. Therefore, with this method porous surfaces act as active media for reversible switching between the sticky and slippery state.

## **MECHANISM OF DROPLET ACTUATION AND MOVEMENT**

### **Depinning of the receding contact line and droplet movement-Computational approach**

To provide insights into the mechanisms of droplet movement, we propose a model that simulates the dynamics of droplet actuation on porous surfaces. The model comprises the momentum conservation equations and the continuity equation along with the Cahn-Hilliard phase-field equations<sup>67, 68</sup> that provide the tracking of the involved phases (liquid-air). The current model is implemented in 2D, due to the relatively low computational cost, where otherwise a full implementation in 3D would yield significantly higher computational costs, restricting more discerning analyses as presented below. The fundamental differences between the 2D and 3D implementations prohibit any strictly quantitative comparison with the experimental data, although we argue that the illuminated mechanisms of droplet movement are valid.

Consider a water droplet with translational symmetry, of height  $\sim 2$  mm wetting a flat surface surrounded by air, inside a 2D computational domain  $\Omega = [6.2, 6.2]$  mm (see Figure 6). The governing equations are the following: 1) The momentum equations including an additional term that accounts for the surface tension force<sup>69</sup>:

$$\rho \frac{\partial \mathbf{u}}{\partial t} + \rho(\mathbf{u} \cdot \nabla) \mathbf{u} = -\nabla p + \mu \nabla^2 \mathbf{u} + \rho \mathbf{g} + G \nabla \varphi \quad \text{Eq. 1}$$

where  $\mathbf{u}$  is the flow velocity vector,  $p$  is the pressure,  $\mathbf{g}$  is the gravitational acceleration,  $G$  is the chemical potential (see below) and  $\varphi$  is the phase-field, i.e. a spatial variable that indicates the present phase; wherever  $\varphi = 1$  indicates the presence of water, whereas  $\varphi = -1$  indicates the presence of air. The density and viscosity depend on  $\varphi$  according to the relations:

$\rho = \frac{1+\varphi}{2} \rho_w + \frac{1-\varphi}{2} \rho_a$  and  $\mu = \frac{1+\varphi}{2} \mu_w + \frac{1-\varphi}{2} \mu_a$ , where  $\rho_a, \mu_a$  are the density and viscosity of air and  $\rho_w, \mu_w$  are the density and viscosity of water. 2) The Cahn-Hilliard phase-field equations<sup>70</sup>:

$$G = \frac{\lambda}{\varepsilon^2} (-\varepsilon^2 \nabla^2 \varphi + \varphi^3 - \varphi) \quad \text{Eq. 2}$$

$$\frac{\partial \varphi}{\partial t} + \nabla \cdot (\varphi \mathbf{u}) = \nabla \cdot (M \nabla G),$$

where,  $\lambda$ , is the mixing energy density that is related to the surface tension through  $\sigma = 2\sqrt{2\lambda/3\varepsilon}$ ,  $\varepsilon$  is the capillary width that controls the thickness of the diffuse interface and  $M$  is the mobility of the diffuse interface. 3) The continuity equation, augmented with a source term that accounts for the air inlet at the pores, which are introduced to the model as point sources of mass:

$$\frac{\partial \rho}{\partial t} + \nabla \cdot (\rho \mathbf{u}) = \sum_i F_a \delta_i \quad \text{Eq. 3}$$

where  $F_a$  is the mass flow rate at which air is entering the computational domain through each point source (pore) and  $\delta_i$  is the Dirac delta function centered at the  $i$ -th pore. The point sources are placed on the flat solid surface, i.e. the bottom boundary of the computational domain, at a

distance of 0.89 mm between each other, even though the pores are numerous and more densely distributed in reality. The compromise of including fewer pores in the model is essential because otherwise, it would require an extremely fine computational mesh that resolves all the point sources. Furthermore, we expect that the inclusion of more pores will not have a considerable effect on the results, due to the fast coalescence of air bubbles formed at the pores (presented below). The individual bubbles at each pore are generally short-lived and eventually coalesce into larger bubbles. Each established bubble is expanded by air entering through all the assimilated pores, which have the equivalent effect of a single pore. This process is also suggested by experimental observations (Figure 4a), where the only observed bubbles are relatively large and countable, even though air is permeating the porous substrate through a significantly large number of pores. In the context of 2D simulations, the point sources (pores) represent infinitesimally narrow slits, extending in the direction of the translational symmetry plane. Therefore, the mass flow rate,  $F_a$ , is defined per unit length of the slits ( $\text{kg}/(\text{s}\cdot\text{m})$ ).

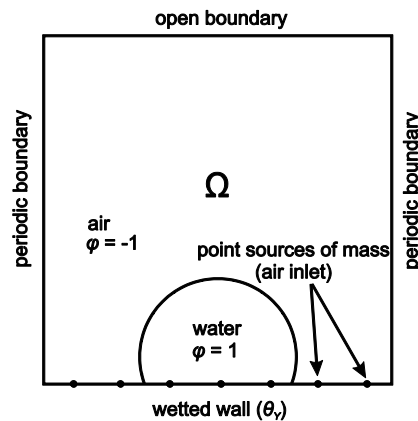


**Figure 6.** Illustration of the 2D computational domain,  $\Omega$ .

Contact angle hysteresis is modeled by periodically varying Young's contact angle,  $\theta_Y$ , along the bottom boundary;  $\theta_Y$  is imposed as a boundary condition of Eq. 2<sup>71</sup>. The value of  $\theta_Y$  follows a square waveform with amplitude  $40^\circ$  around the mean value of  $90^\circ$  and period of 0.31 mm. This approach yields realistic values of contact angle hysteresis  $\sim 20^\circ$ , based on contact angle measurements.

On the vertical boundaries of the computational domain, we impose periodic conditions in order to allow long travelling distances of the droplet, while maintaining a small size of the domain. Finally, the domain,  $\Omega$ , is tessellated into a mesh of  $\sim 32000$  triangular elements and equations (1)-(3) are discretized with a finite element method, utilizing the commercial software package COMSOL Multiphysics (ver. 4.3b). A denser mesh of  $\sim 64000$  elements was also utilized in a mesh sensitivity study for selected values of  $F_a$ , namely  $2.45 \times 10^{-5}$  and  $6.13 \times 10^{-5}$  kg/(s·m). The criterion that satisfies the mesh sensitivity requirements has to be a calculated quantity with statistical significance, given that most of the commonly used variables, e.g. pressure, velocities, etc., fluctuate randomly due to the nature of two-phase flows. We opted for the mean velocity of the center of mass of the droplet (see below) that besides statistical significance has physical importance as well. The refined mesh yielded only up to 5% change in the mean velocities, which for the purposes of this work was deemed negligible and therefore, only the coarser mesh was systematically used.

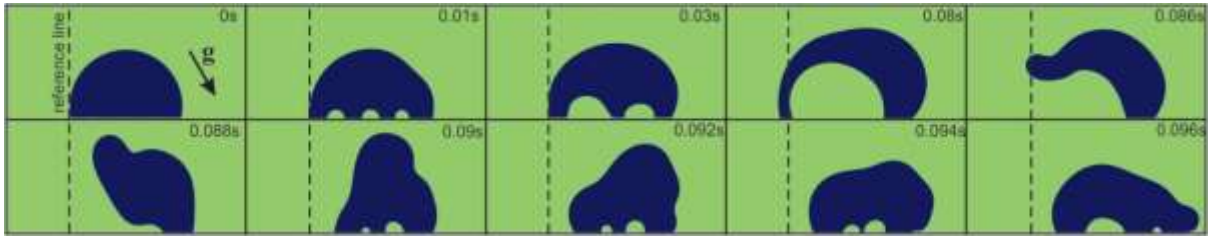


**Figure 7.** Simulation snapshots of droplet lateral movement on an inclined plane (notice the gravitational acceleration) with air permeating the solid substrate. The snapshots include the elapsed time and they are arranged sequentially from left to right and top to bottom. The droplet profile is drawn against a spatially fixed vertical line that provides a reference for the droplet displacement; inclination =  $30^\circ$ ,  $F_a = 2.45 \times 10^{-5}$  kg/(s·m).

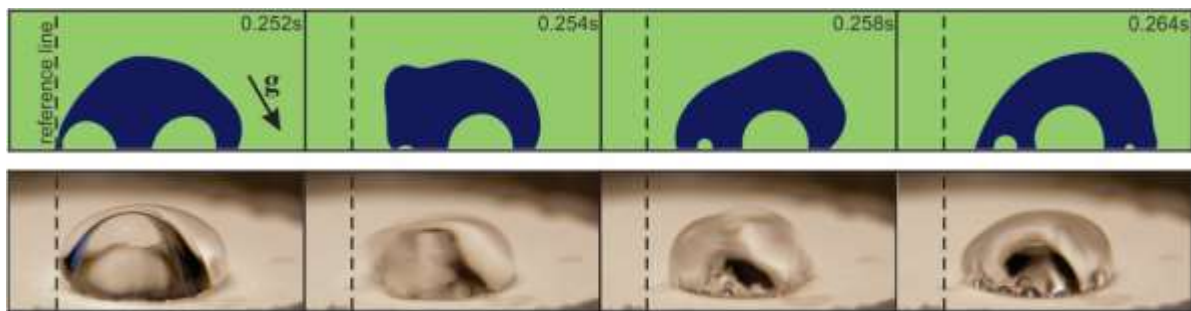


**Figure 8.** Comparison of snapshots from simulation and experiment, illustrating the mechanism of droplet movement. The collapse of the air bubble at the rear of the droplet sends a wave on the droplet surface that is travelling forward and can be seen in both simulations and experiments; the wave in the experiment snapshots is blurry due to the relatively slow camera shutter speed. The simulation snapshots correspond to a later stage of the simulation presented in Figure 7.

In Figure 7 we present simulation snapshots that outline a mechanism of droplet movement. The initial conditions of the simulations include a droplet on an inclined porous surface, not necessarily at an equilibrium state, i.e. the initial conditions are only estimations of the expected equilibrium wetting state. For  $t = 0$  s, we enforce a certain rate in which air permeates the substrate ( $F_a$ ), and

furthermore we allow the effect of gravitational forces. Air pockets are gradually formed and expanded (Figure 7 -  $t = 0.01$  s), some of which coalesce into larger ones (Figure 7 -  $t = 0.03$  s). The droplet remains pinned until the stretched liquid bridge, formed between the outside air and the air pocket (Figure 7 -  $t = 0.08$  s) at the rear of the droplet (with respect to the direction of gravity), collapses. The collapse sends a wave forward on the surface of the droplet that reaches the solid surface on the front of the droplet (Figure 7 -  $t = 0.086$  s to 0.094 s), at which point the droplet gets pinned on the surface (Figure 7 -  $t = 0.096$  s). Eventually, the droplet has skipped forward by the amount of the solid surface length that gets attached to the front of the droplet. This is the mainly observed mechanism of droplet movement that resembles droplet rolling – demonstrated also in Figure 9 (first row), for a later stage ( $t = 0.252 - 0.264$  s). The collapse of the air bubble at the rear of the droplet and the wave on the droplet surface that is travelling forward can be also seen in the experiments as shown in Figure 9 (second row).

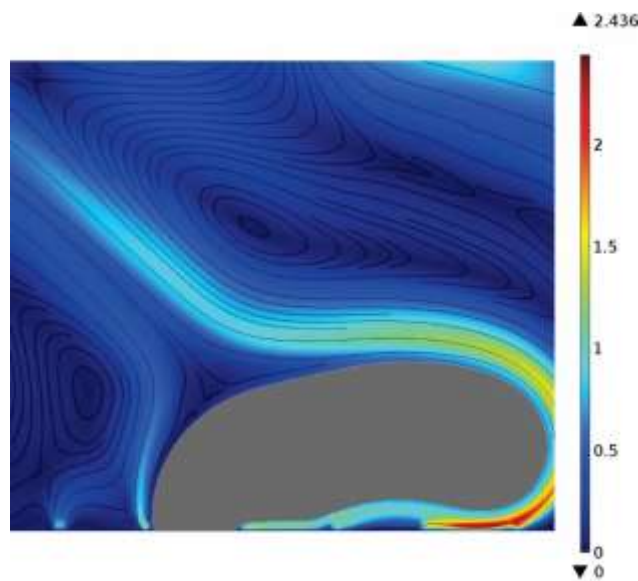


**Figure 9.** Snapshot of a droplet (illustrated in grey color) pinned in the area between two pores, with its bulk suspended on a cushion of air entering through the pores. Streamlines are shown with black lines and the velocity field magnitude (m/s) is illustrated in color scale;  $t = 0.1$  s, inclination =  $30^\circ$ ,  $F_a = 1.22 \times 10^{-4}$  kg/(s·m).

The simulation results shown in Figures 7 and 8 refer to moderate values of  $F_a$ . If however,  $F_a$  reaches a certain limit, we observe levitation of the droplet on its larger part, while a small part of the droplet is pinned to areas of the solid lacking pores (Figure 9). The pinning effectively, binds the droplet to the surface, restricting any lateral movement, which is also illustrated by the velocity of the droplet's center of mass (Figure 10 – blue line). The velocity (component parallel to the surface) of the center of mass fluctuates mildly around 0; the fluctuations are caused by air entering from beneath, inciting droplet oscillations. This macroscopically static behavior has been also identified in the case of droplet motion using vertical vibration on an inclined surface<sup>35, 36</sup>.

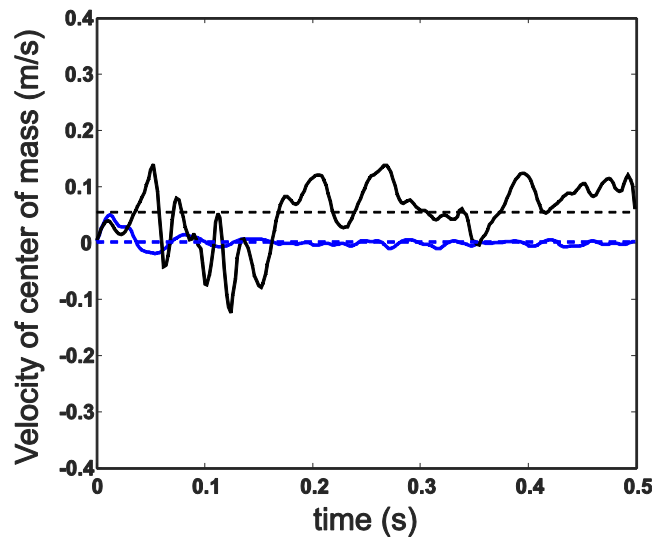


**Figure 10.** Velocity (parallel component to the solid surface) of the droplet's center of mass, versus time. Blue solid line:  $F_a = 1.22 \times 10^{-4}$  kg/(s·m), black solid line:  $F_a = 8.57 \times 10^{-5}$  kg/(s·m). Dashed lines indicate the corresponding (color) mean velocities; inclination =  $30^\circ$ .

Further increase of  $F_a$  causes complete levitation of the droplet and eventually gets ejected upwards, at which point the computations break down, since the droplet leaves the computational domain. For smaller values of  $F_a$ , the velocity fluctuates more aggressively in an almost irregular fashion (Figure 10 – black line) having many instances with the center of mass travelling in the reverse direction (negative velocity), i.e. against gravity. The negative velocity is associated to a brief reversal of the movement mechanism, meaning that a bubble collapse occurs at the front of the droplet (instead of a collapse at the rear), sending a wave in the reverse direction. The reverse mechanism is rarely observed and ultimately has little impact on the mean velocity of the droplet, which has a monotonous increase with  $F_a$  (Figure 11), until the behavior of the system shifts to what was described above and illustrated in Figure 9.

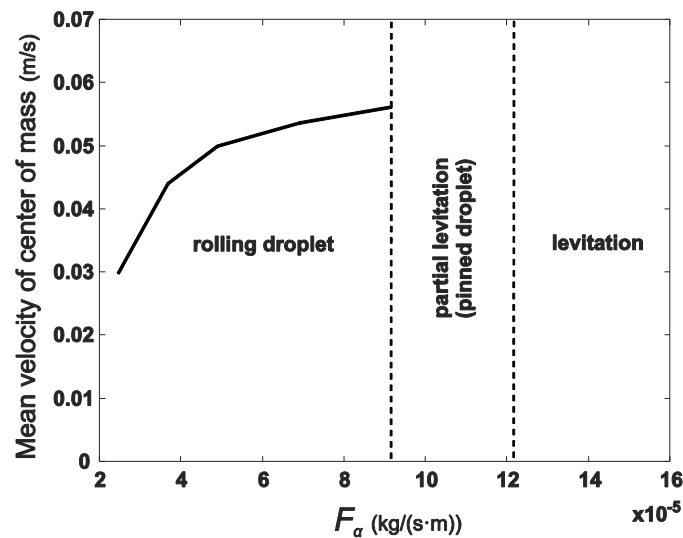


**Figure 11.** Mean velocity (parallel component to the solid surface) of the droplet’s center of mass, versus  $F_a$ . The regime denoted ‘partial levitation’ has effectively zero mean velocity, since the droplet is pinned. Beyond that regime, the droplet levitates completely and computations are no longer feasible (the droplet leaves the computational domain).

## Calculation of the total pinned fraction of the macroscopic contact line

In most cases the mobility of a droplet, and the gradual conversion from a sticky to a slippery state is assessed by measuring the sliding ( $\alpha$ ), i.e. the minimum angle which a surface has to be inclined in order to insemenate moving of the droplet. Many studies have been reported, towards understanding the mechanisms upon droplet movement<sup>72, 73, 74, 75</sup>. The governing equation is actually a balance of forces acting parallel to the surface, namely the gravitational force and the pinning, hysteretic forces at the liquid/solid interface. Exactly at  $\alpha$ , i.e. at the verge of sliding or rolling, the balance takes the form:

$$\rho g V \sin \alpha = k 2 \omega \gamma (\cos \theta_r - \cos \theta_a) \quad \text{Eq. 4}$$

where  $\rho$  and  $\gamma$  is the density and surface tension of the liquid, respectively,  $V$  the droplet volume,  $2\omega$  is the width of the drop in the direction perpendicular to inclination,  $k$  is a retention-force factor, which is expected to be equal to 1, but is usually adjusted to fit the experimental data.  $\theta_r$  and  $\theta_a$  are the receding and advancing contact angle, respectively, of the droplet on the respective smooth solid surface.

Discrepancies from this expression of force balance are far from rare, due to different theoretical assumptions or different conditions for the experiments<sup>75, 76, 77, 78</sup>, while in this form it cannot explicitly account for the contributions of the capillary bridges developed in textured surfaces<sup>51</sup>.

A different approach in treating this problem is provided by assuming the in-plane retention forces<sup>75, 79</sup> or the vertical pinning forces at the receding contact line<sup>78</sup> for each capillary bridge. In this latter approach the vertical pinning force for each ( $j$ ) capillary bridge is given by:

$$F_j = P_j \gamma \sin(\theta_r^j) \quad \text{Eq. 5}$$

where  $P_j$  is the perimeter of an individual surface feature, and  $\theta_r^j$  is the receding angle local to the  $j^{\text{th}}$  feature. Contrary to the in-plane pinning forces appeared in Eq. 4, this approach yields the adhesion in the vertical direction:

$$F/l = \Phi_0 \gamma \sin(\theta_r) \quad \text{Eq. 6}$$

where  $\Phi_0$  is the total pinned fraction of a macroscopic contact line, and can be considered as a multiplier reflecting the strength of pinning on the textured surface compared to the respective smooth surface.  $l$  is the length of the macroscopic projected contact line.

We are going to employ the model developed by Paxson et al<sup>78</sup> accounting also for the vertical forces of each capillary bridge at the receding contact line, with appropriate modifications in order to account for the effect of the backpressure.  $F_L$  is the force due to the Laplace pressure:

$$F_L = |r_b^2 \left(\frac{2\gamma}{r}\right) \quad \text{Eq. 7}$$

where  $r_b$  is the radius of the contact patch, and  $r$  is the droplet radius.

$F_S$  is the force due to the surface tension acting along the peripheral roughness features:

$$F_S = 2 |r_b \Phi_0 \gamma \sin(\theta_r) \quad \text{Eq. 8}$$

$\Phi_0$  is actually the fraction of the pinned contact line, and can be considered as a multiplier reflecting the strength of pinning on the textured surface compared to the respective smooth surface.

In all cases the gravitational force ( $F_G$ ) is given by:

$$F_G = \rho g V \quad \text{Eq. 9}$$

The exact number of  $r_b$  and  $\Phi_0$ , before, and after, backpressure application, cannot be readily measured experimentally, and therefore assumptions will be drawn. Based on the SEM image given in Figure 1, the vast majority of  $r_b$  ranges from ca. 0.50  $\mu\text{m}$  to 1.65  $\mu\text{m}$ . Since the particles do not exhibit additional scale roughness it is reasonable to take  $\Phi_0$  equal or close to 1.

For a water droplet of 20  $\mu\text{l}$ , exhibiting  $r=1.68$  mm, well below the capillary length  $l_c = \sqrt{\gamma/\rho g} \approx 2.7$  mm, before the backpressure application, for  $\gamma=0.073$  N/m,  $\theta_r = 92^\circ$ ,  $r_b = 1.07$   $\mu\text{m}$  and  $\Phi_0$  equal to 1, the pertinent forces are:

$F_L = 3.12 \cdot 10^{-10}$  N and based on the variation of  $r_b$ ,  $F_L$  may range from 0.682  $\cdot 10^{-10}$  N to 7.34  $\cdot 10^{-10}$  N

$F_S = 4.90 \cdot 10^{-7}$  N, and based on the variation of  $r_b$ ,  $F_S$  may range from 2.29  $\cdot 10^{-7}$  N to 7.51  $\cdot 10^{-7}$  N

Clearly  $F_L$  is by three orders of magnitude smaller than  $F_S$ , therefore we are going to neglect it in the analysis hereafter.

The gradual increase of backpressure, exerting a force  $F_p$ , on a quiescent droplet at a hydrophobic and inherently sticky incline introduces manifold changes in the principle vertical force balance. A schematic of this process is given in Figure 12. With the application of the backpressure not only  $F_p$  is introduced in the force balance but also the radius of the contact patch  $r_b$  decreases to  $r'_b$ , while  $\theta_r$  decreases to  $\theta'_r$ .

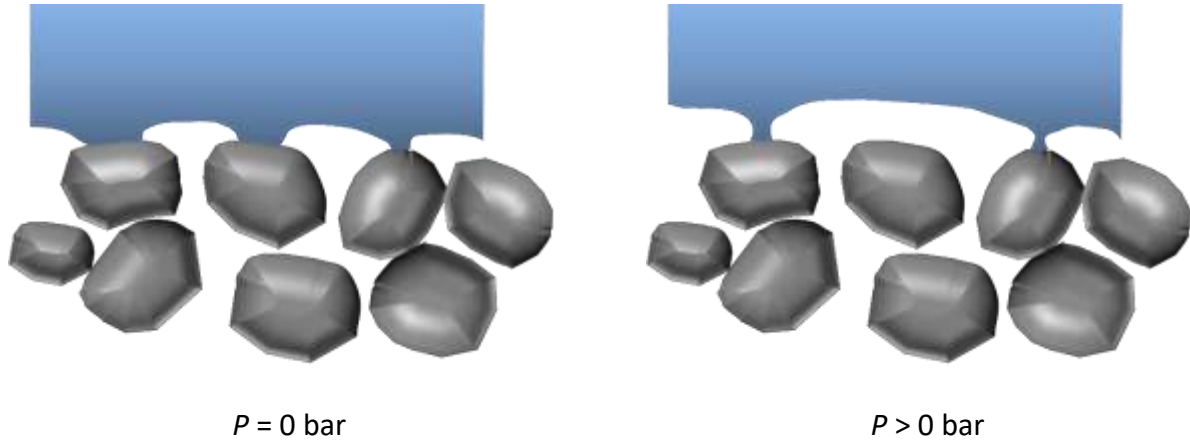


**Figure 12.** Schematic of the envisaged microscopic apparent contact line and capillary bridges atop the porous network.

For a 20  $\mu\text{l}$  water droplet the adequate pressure for sliding on a horizontal plane is 0.78 bar. Based on the SEM image in Figure 1, the pore radius ranges from ca. 0.5  $\mu\text{m}$  to ca. 1.6  $\mu\text{m}$ . Taking the average, 1.05  $\mu\text{m}$ ,  $F_p$  yields:

$F_p = P A = 2.68 \cdot 10^{-9}$  N, with  $A$  being the pore opening area, and based on the variation of the pore size  $F_p$  may range from  $6.08 \cdot 10^{-10}$  N to  $6.23 \cdot 10^{-9}$  N.

Since we cannot measure the exact  $r'_b$  and  $\theta'_r$ , we are going to calculate the total pinned fraction of the contact line after backpressure application,  $\Phi'_0$ , as the multiplier accounting for the decrease of  $F_S$  to  $F'_S$ , encompassing the variations of  $r_b$  and  $\theta_r$ .  $\Phi'_0 = \frac{2.68 \cdot 10^{-9}}{4.90 \cdot 10^{-7}} = 5.5 \cdot 10^{-3}$ , which is two to three order of magnitudes lower compared to the initial state. This value corroborates the mechanism revealed by the numerical approach presented before, entailing the partial depinning of the receding contact line, which triggers the droplet actuation. The reduction of the pinned fraction is supported also experimentally, see Figure 4a (III)-(IV).

For bigger droplets the in-plane gravitational force is higher and therefore, a lower depinning fraction is needed to incite the downward movement, reflected by smaller backpressure values.

The differences recorded for the case of ethanol in water cannot be attributed only to the effect of  $\gamma$ . The decrease of  $\gamma$  is of ca. 40% (0.073 to 0.045 N/m), whereas the backpressure lowering is more than 77% (e.g. for a 50  $\mu\text{l}$  droplet at zero inclination 0.60 to 0.14 bar). The differences in this case stem on the different contact patch radius ( $r_b$ ) of the two liquids on the porous surfaces. Water and ethanol in water liquids are expected to exhibit different intrusion angle<sup>80</sup>, thus corresponding to different  $r_b$ , which is in turn is reflected in the vertical force balance.

## CONCLUSIONS

We provided insights on the underlying mechanisms of droplet actuation on porous media by means of backpressure and surface inclination; the latter are combined to facilitate active control of droplet mobility. Adjusting the porous backpressure the droplet may be pinned to the surface or may be actuated and move downwards by the presence of a small inclination. The interplay between backpressure and inclination has been quantified for various volumes of DI water and ethanol in DI water droplets. Actuation and mobility control may be realized without a fully developed air cushion under the liquid; therefore Leidenfrost-like dynamics cannot be used. Simulations have shown that the droplet is actuated through a depinning process of the receding contact line and moves by means of forward wave propagation towards the front contact line. The droplet shapes obtained by this numerical approach are fairly compared to the ones observed experimentally, thus providing a reasonable justification of this approach. The small openings observed experimentally at the contact line during movement are followed by means of an analytical approach accounting for the vertical force balance and the total pinning fraction.

## Acknowledgements

NV and VS have received funding from the European Union's Horizon 2020 research and innovation programme under grant agreement No 680599 (Project Title: Industrial Thermal Energy Recovery Conversion and Management). GP, GK and AB have received funding from the Hellenic National Strategic Reference Framework (NSRF) 2007-2013 under grant agreement No MIS380835 (Project Title: THALES – DESIREDROP: DESIgn and fabrication of Robust superhydrophobic/hydrophilic surfaces and their application in the realization of “smart” microfluidic valves).

## REFERENCES

1. de Gennes, P. G.; Brochard-Wyart, F.; Quere, D. *Capillarity and Wetting Phenomena: Drops, Bubbles, Pearls, Waves*; Springer-Verlag: New York, 2004.
2. Glavan, A. C.; Martinez, R. V.; Maxwell, E. J.; Subramaniam, A. B.; Nunes, R. M.; Soh, S.; Whitesides, G. M. Rapid fabrication of pressure-driven open-channel microfluidic devices in omniphobic R(F) paper. *Lab on a chip* **2013**, *13* (15), 2922-30.
3. Vourdas, N.; Tserepi, A.; Boudouvis, A.; Gogolides, E. Plasma processing for polymeric microfluidics fabrication and surface modification: Effect of super-hydrophobic walls on electroosmotic flow. *Microelectronic Engineering* **2008**, *85* (5), 1124-1127.
4. Moschou, D.; Vourdas, N.; Kokkoris, G.; Papadakis, G.; Parthenios, J.; Chantzandroulis, S.; Tserepi, A. All-plastic, low-power, disposable, continuous-flow PCR chip with integrated microheaters for rapid DNA amplification. *Sensors and Actuators B: Chemical* **2014**, *199*, 470-478.
5. Kitsara, M.; Ducrée, J. Integration of functional materials and surface modification for polymeric microfluidic systems. *Journal of Micromechanics and Microengineering* **2013**, *23* (3), 033001.
6. Ghosh, A.; Ganguly, R.; Schutzius, T. M.; Megaridis, C. M. Wettability patterning for high-rate, pumpless fluid transport on open, non-planar microfluidic platforms. *Lab on a chip* **2014**, *14* (9), 1538-1550.
7. Abdelgawad, M.; Freire, S. L. S.; Yang, H.; Wheeler, A. R. All-terrain droplet actuation. *Lab on a chip* **2008**, *8* (5), 672-677.
8. Gogolides, E.; Ellinas, K.; Tserepi, A. Hierarchical micro and nano structured, hydrophilic, superhydrophobic and superoleophobic surfaces incorporated in microfluidics, microarrays and lab on chip microsystems. *Microelectronic Engineering* **2015**, *132*, 135-155.
9. Song, H.; Chen, D. L.; Ismagilov, R. F. Reactions in droplets in microfluidic channels. *Angewandte Chemie* **2006**, *45* (44), 7336-56.

10. Abdelaziz, R.; Disci-Zayed, D.; Hedayati, M. K.; Pöhls, J.-H.; Zillohu, A. U.; Erkartal, B.; Chakravadhanula, V. S. K.; Duppel, V.; Kienle, L.; Elbahri, M. Green chemistry and nanofabrication in a levitated Leidenfrost drop. *Nature communications* **2013**, *4*, 2400.
11. Vourdas, N.; Tserepi, A.; Gogolides, E. Nanotextured super-hydrophobic transparent poly (methyl methacrylate) surfaces using high-density plasma processing. *Nanotechnology* **2007**, *18* (12), 125304.
12. Vourdas, N. E.; Vlachopoulou, M. E.; Tserepi, A.; Gogolides, E. Nano-textured polymer surfaces with controlled wetting and optical properties using plasma processing. *International Journal of Nanotechnology* **2009**, *6* (1-2), 196-207.
13. Tsougeni, K.; Vourdas, N.; Tserepi, A.; Gogolides, E.; Cardinaud, C. Mechanisms of oxygen plasma nanotexturing of organic polymer surfaces: from stable super hydrophilic to super hydrophobic surfaces. *Langmuir* **2009**, *25* (19), 11748-11759.
14. Gogolides, E.; Vlachopoulou, M.; Tsougeni, K.; Vourdas, N.; Tserepi, A. Micro and nano structuring and texturing of polymers using plasma processes: potential manufacturing applications. *International Journal of Nanomanufacturing* **2010**, *6* (1), 152-163.
15. Schutzius, T. M.; Jung, S.; Maitra, T.; Eberle, P.; Antonini, C.; Stamatopoulos, C.; Poulikakos, D. Physics of Icing and Rational Design of Surfaces with Extraordinary Icephobicity. *Langmuir* **2014**, *31* (17), 4807-4821.
16. Davis, A.; Yeong, Y. H.; Steele, A.; Bayer, I. S.; Loth, E. Superhydrophobic Nanocomposite Surface Topography and Ice Adhesion. *ACS Applied Materials & Interfaces* **2014**, *6* (12), 9272-9279.
17. Mosadegh-Sedghi, S.; Rodrigue, D.; Brisson, J.; Iliuta, M. C. Wetting phenomenon in membrane contactors – Causes and prevention. *Journal of Membrane Science* **2014**, *452*, 332-353.
18. Cheah, M. J.; Kevrekidis, I. G.; Benziger, J. B. Water slug formation and motion in gas flow channels: the effects of geometry, surface wettability, and gravity. *Langmuir* **2013**, *29* (31), 9918-9934.
19. Zhang, F. Y.; Yang, X. G.; Wang, C. Y. Liquid water removal from a polymer electrolyte fuel cell. *Journal of the Electrochemical Society* **2006**, *153* (2), A225-A232.
20. Ghosh, A.; Beaini, S.; Zhang, B. J.; Ganguly, R.; Megaridis, C. M. Enhancing Dropwise Condensation through Bioinspired Wettability Patterning. *Langmuir* **2014**, *30* (43), 13103-13115.
21. Attinger, D.; Frankiewicz, C.; Betz, A. R.; Schutzius, T. M.; Ganguly, R.; Das, A.; Kim, C.-J.; Megaridis, C. M. Surface engineering for phase change heat transfer: A review. *MRS Energy & Sustainability* **2014**, *1*, E4.
22. Khalil, K. S.; Mahmoudi, S. R.; Abu-dheir, N.; Varanasi, K. K. Active surfaces: Ferrofluid-impregnated surfaces for active manipulation of droplets. *Applied Physics Letters* **2014**, *105* (4), 041604.
23. Zhu, Y.; Antao, D. S.; Xiao, R.; Wang, E. N. Tunable Surfaces: Real-Time Manipulation with Magnetically Tunable Structures (Adv. Mater. 37/2014). *Advanced Materials* **2014**, *26* (37), 6357-6357.
24. Yao, X.; Hu, Y.; Grinthal, A.; Wong, T. S.; Mahadevan, L.; Aizenberg, J. Adaptive fluid-infused porous films with tunable transparency and wettability. *Nature Materials* **2013**, *12*, 529-534.
25. Stamatopoulos, C.; Schutzius, T. M.; Köppl, C. J.; El Hayek, N.; Maitra, T.; Hemrle, J.; Poulikakos, D. On the shedding of impaled droplets: The role of transient intervening layers. *Scientific reports* **2016**, *6*, 18875.
26. Verplanck, N.; Coffinier, Y.; Thomy, V.; Boukherroub, R. Wettability Switching Techniques on Superhydrophobic Surfaces. *Nanoscale Research Letters* **2007**, *2* (12), 577-596.
27. Reyssat, M.; Richard, D.; Clanet, C.; Quere, D. Dynamical superhydrophobicity. *Faraday Discussions* **2010**, *146*, 19-33.
28. Whyman, G.; Bormashenko, E. Wetting transitions on rough substrates: General considerations. *Journal of Adhesion Science and Technology* **2012**, *26*, 207-220.
29. Bormashenko, E.; Musin, A.; Whyman, G.; Zinigrad, M. Wetting Transitions and Depinning of the Triple Line. *Langmuir* **2012**, *28* (7), 3460-3464.
30. Bormashenko, E. Progress in understanding wetting transitions on rough surfaces. *Advances in colloid and interface science* **2014**, *222*, 92-103.
31. Krupenkin, T. N.; Taylor, J. A.; Wang, E. N.; Kolodner, P.; Hodes, M.; Salamon, T. R. Reversible Wetting-Dewetting Transitions on Electrically Tunable Superhydrophobic Nanostructured Surfaces. *Langmuir* **2007**, *23* (18), 9128-9133.

32. Zhang, J.; Feng, H.; Zao, W.; Zhao, Y.; Zhang, H.; Liu, Y. Magnetically driven superhydrophobic meshes with the capacity of moving at air/water and oil/water interfaces. *RSC Advances* **2015**, *5* (59), 47892-47899.
33. Sammarco, T. S.; Burns, M. A. Thermocapillary pumping of discrete drops in microfabricated analysis devices. *AIChE Journal* **1999**, *45* (2), 350-366.
34. Boreyko, J. B.; Collier, C. P. Dewetting Transitions on Superhydrophobic Surfaces: When Are Wenzel Drops Reversible? *The Journal of Physical Chemistry C* **2013**, 130826065303007.
35. Sartori, P.; Quagliati, D.; Varagnolo, S.; Pierno, M.; Mistura, G.; Magaletti, F.; Casciola, C. M. Drop motion induced by vertical vibrations. *New Journal of Physics* **2015**, *17* (11), 113017.
36. Brunet, P.; Eggers, J.; Deegan, R. D. Vibration-induced climbing of drops. *Physical review letters* **2007**, *99* (14), 144501.
37. Lee, J.; He, B.; Patankar, N. A. A roughness-based wettability switching membrane device for hydrophobic surfaces. *Journal of Micromechanics and Microengineering* **2005**, *15* (3), 591.
38. Park, S.-Y.; Chiou, P.-Y. Light-driven droplet manipulation technologies for lab-on-a-chip applications. *Advances in OptoElectronics* **2011**, 2011.
39. Jin, M.; Li, S.; Wang, J.; Xue, Z.; Liao, M.; Wang, S. Underwater superoleophilicity to superoleophobicity: role of trapped air. *Chemical Communications* **2012**, *48* (96), 11745-11747.
40. de Ruitter, J.; Lagraauw, R.; van den Ende, D.; Mugele, F. Wettability-independent bouncing on flat surfaces mediated by thin air films. *Nat Phys* **2014**, *11* (1), 48-53.
41. Vourdas, N.; Tserepi, A.; Stathopoulos, V. N. Reversible pressure-induced switching of droplet mobility after impingement on porous surface media. *Applied Physics Letters* **2013**, *103* (11), 111602.
42. Bouwhuis, W.; Hendrix, M. H. W.; van der Meer, D.; Snoeijer, J. H. Initial surface deformations during impact on a liquid pool. *Journal of Fluid Mechanics* **2015**, *771*, 503- 519.
43. Schutzius, T. M.; Jung, S.; Maitra, T.; Graeber, G.; Köhme, M.; Poulikakos, D. Spontaneous droplet trampolining on rigid superhydrophobic surfaces. *Nature* **2015**, *527* (7576), 82-85.
44. Lee, C.; Kim, C.-J. Underwater Restoration and Retention of Gases on Superhydrophobic Surfaces for Drag Reduction. *Physical Review Letters* **2011**, *106* (1), 014502.
45. Verho, T.; Korhonen, J. T.; Sainiemi, L.; Jokinen, V.; Bower, C.; Franze, K.; Franssila, S.; Andrew, P.; Ikkala, O.; Ras, R. H. A. Reversible switching between superhydrophobic states on a hierarchically structured surface. *Proceedings of the National Academy of Sciences* **2012**, *109* (26), 10210–10213.
46. Tan, J. N.; Ling, W. Y. L.; Neild, A. Selective Liquid Droplet Transfer Using Injected Bubbles. *Applied Physics Express* **2013**, *6* (7), 077301.
47. Karatay, E.; Haase, A. S.; Visser, C. W.; Sun, C.; Lohse, D.; Tsai, P. A.; Lammertink, R. G. Control of slippage with tunable bubble mattresses. *Proceedings of the National Academy of Sciences of the United States of America* **2013**, *110* (21), 8422-6.
48. Antonini, C.; Carmona, F. J.; Pierce, E.; Marengo, M.; Amirfazli, A. General methodology for evaluating the adhesion force of drops and bubbles on solid surfaces. *Langmuir* **2009**, *25* (11), 6143-54.
49. Ling, W. Y.; Lu, G.; Ng, T. W. Increased stability and size of a bubble on a superhydrophobic surface. *Langmuir* **2011**, *27* (7), 3233-7.
50. Ling, W. Y.; Ng, T. W.; Neild, A. Effect of an encapsulated bubble in inhibiting droplet sliding. *Langmuir* **2010**, *26* (22), 17695-702.
51. Liang Ling, W. Y.; Ng, T. W.; Neild, A.; Zheng, Q. Sliding variability of droplets on a hydrophobic incline due to surface entrained air bubbles. *J Colloid Interface Sci* **2011**, *354* (2), 832-42.
52. Goldshtik, M. A.; Khanin, V. M.; Ligai, V. G. A liquid drop on an air cushion as an analogue of Leidenfrost boiling. *Journal of Fluid Mechanics* **1986**, *166*, 1-20.
53. Brunet, P.; Snoeijer, J. H. Star-drops formed by periodic excitation and on an air cushion – A short review. *The European Physical Journal Special Topics* **2011**, *192* (1), 207-226.
54. Bouwhuis, W.; Winkels, K. G.; Peters, I. R.; Brunet, P.; van der Meer, D.; Snoeijer, J. H. Oscillating and star-shaped drops levitated by an airflow. *Physical Review E* **2013**, *88* (2), 023017.
55. Papoular, M.; Parayre, C. Gas-film levitated liquids: Shape fluctuations of viscous drops. *Physical Review Letters* **1997**, *78* (11), 2120-2123.

56. Vourdas, N.; Ranos, C.; Stathopoulos, V. N. Reversible and dynamic transitions between sticky and slippery states on porous surfaces with ultra-low backpressure. *RSC Advances* **2015**, *5* (42), 33666-33673.
57. Vourdas, N.; Stathopoulos, V. N. Droplet actuation and droplet mobility manipulation on porous surfaces by means of backpressure control. In *Technical Proceedings of the 2014 NSTI Nanotechnology Conference and Expo, NSTI-Nanotech 2014*, 2014; Vol. 1, pp 220-223.
58. Stathopoulos, V. N.; Vourdas, N. Reversible wetting transitions on porous materials. In *The 8th International Conference on Material Technologies and Modeling, MMT 2014*, 2014, pp 4-144.
59. Vourdas, N.; Dalamagkidis, K.; Stathopoulos, V. Active porous valves for plug actuation and plug flow manipulation in open channel fluidics. *RSC Advances* **2015**, *5* (126), 104594-104600.
60. Vourdas, N.; Dalamagkidis, K.; Stathopoulos, V. N. uVALVIT: A tool for droplet mobility control and valving. *MATEC Web of Conferences* **2016**, *41*.
61. Quéré, D. Leidenfrost Dynamics. *Annual Review of Fluid Mechanics* **2013**, *45* (1), 197-215.
62. Snoeijer, J.; Brunet, P.; Eggers, J. Maximum size of drops levitated by an air cushion. *Physical Review E* **2009**, *79* (3), 036307.
63. Snoeijer, J. H.; van der Weele, K. Physics of the granite sphere fountain. *American Journal of Physics* **2014**, *82* (11), 1029-1039.
64. Vourdas, N.; Dalamagkidis, K.; Kostis, I.; Vasilopoulou, M.; Davazoglou, D. Omnidirectional antireflective properties of porous tungsten oxide films with in-depth variation of void fraction and stoichiometry. *Optics Communications* **2012**, *285* (24), 5229-5234.
65. Kostis, I.; Vasilopoulou, M.; Soultati, A.; Argitis, P.; Konofaos, N.; Douvas, A. M.; Vourdas, N.; Papadimitropoulos, G.; Davazoglou, D. Highly porous tungsten oxides for electrochromic applications. *Microelectronic Engineering* **2013**, *111*, 149-153.
66. Tan, J. N.; Ma, C.; Sivanantha, N.; Neild, A. Bubble inducing cell lysis in a sessile droplet. *Applied Physics Letters* **2014**, *104* (10), 103704.
67. Pashos, G.; Kokkoris, G.; Boudouvis, A. G. Minimum energy paths of wetting transitions on grooved surfaces. *Langmuir* **2015**, *31* (10), 3059-3068.
68. Pashos, G.; Kokkoris, G.; Boudouvis, A. G. A modified phase-field method for the investigation of wetting transitions of droplets on patterned surfaces. *Journal of Computational Physics* **2015**, *283*, 258-270.
69. Yue, P.; Zhou, C.; Feng, J. J.; Ollivier-Gooch, C. F.; Hu, H. H. Phase-field simulations of interfacial dynamics in viscoelastic fluids using finite elements with adaptive meshing. *Journal of Computational Physics* **2006**, *219* (1), 47-67.
70. Jacqmin, D. Calculation of two-phase Navier-Stokes flows using phase-field modeling. *Journal of Computational Physics* **1999**, *155* (1), 96-127.
71. Lee, H. G.; Kim, J. Accurate contact angle boundary conditions for the Cahn-Hilliard equations. *Computers & Fluids* **2011**, *44* (1), 178-186.
72. Furmidge, C. G. L. Studies at phase interfaces. I. The sliding of liquid drops on solid surfaces and a theory for spray retention. *Journal of Colloid Science* **1962**, *17* (4), 309-324.
73. Quéré, D.; Azzopardi, M.-J.; Delattre, L. Drops at Rest on a Tilted Plane. *Langmuir* **1998**, *14* (8), 2213-2216.
74. Krasovitski, B.; Marmur, A. Drops down the hill: Theoretical Study of Limiting Contact Angles and the Hysteresis Range on a Tilted Plate. *Langmuir* **2005**, *21*, 3881-3885.
75. Extrand, C. W.; Moon, S. I. Repellency of the Lotus Leaf: Contact Angles, Drop Retention, and Sliding Angles. *Langmuir* **2014**, *30* (29), 8791-8797.
76. Santos, M. J.; Velasco, S.; White, J. A. Simulation Analysis of Contact Angles and Retention Forces of Liquid Drops on Inclined Surfaces. *Langmuir* **2012**, *28* (32), 11819-11826.
77. Smyth, K. M.; Varanasi, K. K.; Kwon, H.-M.; Paxson, A. T. Visualization of contact line motion on hydrophobic textures. *Surface Innovations* **2013**, *1* (2), 84-91.
78. Paxson, A. T.; Varanasi, K. K. Self-similarity of contact line depinning from textured surfaces. *Nature communications* **2013**, *4*, 1492.

79. Pilat, D. W.; Papadopoulos, P.; Schaffel, D.; Vollmer, D.; Berger, R.; Butt, H. J. Dynamic measurement of the force required to move a liquid drop on a solid surface. *Langmuir* **2012**, *28* (49), 16812-20.
80. Extrand, C. W.; Moon, S. I. Intrusion pressure to initiate flow through pores between spheres. *Langmuir* **2012**, *28* (7), 3503-3509.